PHYSICAL REVIEW B **91**, 205430 (2015)

Atomic and electronic structure of bismuth-bilayer-terminated $Bi_2Se_3(0001)$ prepared by atomic hydrogen etching

Roozbeh Shokri,[1] Holger L. Meyerheim,[1,*] Sumalay Roy,[1] Katayoon Mohseni,[1] A. Ernst,[1] M. M. Otrokov,[2,3] E. V. Chulkov,[2,3,4] and J. Kirschner[1,5]

[1]*Max-Planck-Institut für Mikrostrukturphysik, Weinberg 2, D-06120 Halle, Germany*

[2]*Tomsk State University, 634050 Tomsk, Russia*

[3]*Donostia International Physics Center (DIPC), 20018 San Sebastián/Donostia, Basque Country, Spain*

[4]*Departamento de Física de Materiales UPV/EHU, Centro de Física de Materiales CFM - MPC and Centro Mixto CSIC-UPV/EHU, 20080 San Sebastián/Donostia, Basque Country, Spain*

[5]*Institut für Physik, Martin-Luther-Universität Halle-Wittenberg, D-06099 Halle, Germany*

(Received 9 January 2015; revised manuscript received 23 April 2015; published 21 May 2015)

A bilayer of bismuth is recognized as a prototype two-dimensional topological insulator. Here we present a simple and well reproducible top-down approach to prepare a flat and well ordered bismuth bilayer with a lateral size of several hundred nanometers on $Bi_2Se_3(0001)$. Using scanning tunneling microscopy, surface x-ray diffraction, and Auger electron spectroscopy we show that exposure of $Bi_2Se_3(0001)$ to atomic hydrogen completely removes selenium from the top quintuple layer. The band structure of the system, calculated from first principles for the experimentally derived atomic structure, is in excellent agreement with recent photoemission data. Our results open interesting perspectives for the study of topological insulators in general.

DOI: 10.1103/PhysRevB.91.205430 PACS number(s): 61.05.cp, 71.15.Mb, 73.20.At, 79.60.−i

I. INTRODUCTION

The discovery of three-dimensional (3D) topological insulators (TIs) has led to intense research owing to the potential applications of these materials in the field of spintronics and quantum computing [1–6]. While TIs are insulating materials in the bulk, they host metallic surface states in the bulk energy gap with a Dirac-cone-like dispersion. Being protected by time-reversal symmetry, these states show spin-momentum locking, which leads to suppression of the electron backscattering by defects. Although theoretically predicted earlier [7], two-dimensional (2D) TIs have been much less investigated. They are characterized by 1D edge states for which first experimental evidence was given by the observation of quantized conductance in HgTe/CdTe semiconductor quantum well structures [8,9]. Since large spin-orbit coupling is a prerequisite for a material to exhibit topologically protected states, bismuth is a primary candidate and bismuth bilayers (BLs) have become under intense study. They are now regarded as a prototype of an elemental 2D TI [10,11]. Recent studies have aimed to prepare bismuth BLs by using different methods such as molecular beam epitaxy [12–15], exfoliation [16], or by investigating step edges of a Bi(111) surface [17].

While these attempts used bottom-up schemes to prepare bismuth BLs leading to films of quite limited size and flatness, in this study, we present a simple and controllable approach, which is based on exposing $Bi_2Se_3(0001)$ to a flux of atomic hydrogen. Our top-down procedure results in a bismuth BL, which is atomically flat and which is limited in lateral size only by the size of the substrate terraces (typically several hundred nanometers). Scanning tunneling microscopy (STM) in combination with surface x-ray diffraction (SXRD) and Auger electron spectroscopy (AES) provide unambiguous evidence for the complete removal of selenium from the first quintuple layer (QL). Only trace amounts (≈0.05 monolayers) of vacancies and bismuth BL islands are found on the surface. The surface energy band dispersion, calculated from first principles for the experimentally obtained crystalline structure, is in excellent agreement with a recent photoemission experiment. Our results open wide perspectives for the study of 2D TIs and for the controlled growth of 3D TI architectures.

II. EXPERIMENT

Bulk Bi_2Se_3 single crystals were grown by the Bridgman method. Crystals were transferred into ultra high vacuum (UHV) (base pressure $\approx 1 \times 10^{-10}$ mbar) and cleaned by mild Ar^+ sputtering (0.5–1 keV) followed by annealing at 450–550 °C for several minutes. STM and AES measurements indicate a well ordered and clean surface with atomically flat terraces up to several hundred nanometers wide. Well contrasted sharp spots evidencing threefold symmetry according to the $p3m1$ plane group symmetry of the surface were observed by low-energy electron diffraction (LEED). Recent SXRD studies of the as prepared surface [18,19] found no evidence for the presence of a bismuth BL termination previously reported for Bi_2Se_3 [20].

Atomic hydrogen was generated by a microwave-driven (2.45 GHz), SPECS PCS-ECR plasma source, operated in the atom-beam mode [21,22]. During the operation of the atom source, the hydrogen partial pressure in the chamber was $p_{H_2} \approx 5 \times 10^{-5}$ mbar. For the quantification of the exposure of the sample, we use Langmuir (L) units ($1\ \mathrm{L} = 1.0 \times 10^{-6}$ Torr s) in the following, which is proportional to the amount of hydrogen atoms interacting with the sample. The sample was kept at room temperature. SXRD experiments were carried out using an in-house UHV diffractometer allowing *in situ* sample preparation and characterization by LEED and AES. A microfocus x-ray source ($\lambda = 1.54$ Å) and

*Electronic address: hmeyerhm@mpi-halle.de

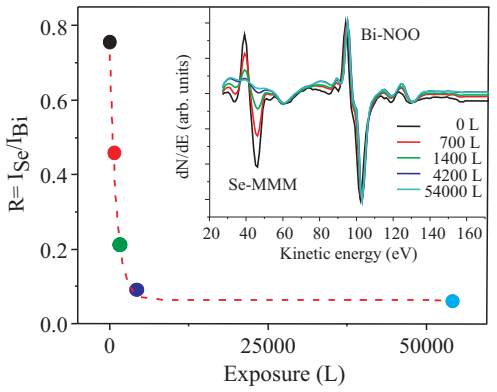

FIG. 1. (Color online) Ratio $R = I_{\text{Se-MMM}}/I_{\text{Bi-NOO}}$ between the peak to peak intensities of the Se-MMM and the Bi-NOO transition vs exposure in Langmuirs. The dashed line is a guide to the eye. The inset shows the corresponding differential AES spectra. Peaks at 42 and 96/101 eV correspond to Se-MMM and Bi-NOO electronic transitions, respectively. Spectra are normalized to the Bi-NOO peak.

a two-dimensional pixel detector were used for the collection of the reflected intensities along the integer order crystal truncation rods (CTRs).

The surface chemistry of the Bi_2Se_3 crystal was analyzed by AES. The inset of Fig. 1 shows a series of differential spectra as a function of the hydrogen exposure. The spectra are dominated by two unresolved Se-MMM Coster-Kronig transitions at a kinetic energy of approximately 43 eV and the Bi-NOO transition 101 eV. In Fig. 1, the intensities are normalized to the Bi-NOO peak. Upon exposure to atomic hydrogen the Se-MMM Auger peak rapidly diminishes. Figure 1 also shows the ratio $R = I_{\text{Se-MMM}}/I_{\text{Bi-NOO}}$ versus exposure. The ratios $R = 0.75$, 0.46, 0.23, 0.09, and 0.06 correspond to the exposures of 0, 700, 1400, 4200, and 54 000 L.

Two regimes can be distinguished, namely the first where R rapidly decreases, and the second, where R is almost constant. The boundary between the regimes lies at approximately 4200 L. The rapid reduction of the selenium peak is attributed to the removal of selenium from the near surface region, creating a bismuth enriched surface. We suggest that selenium atoms are removed via the reaction $2H + Se \rightarrow H_2Se\uparrow$.

Figures 2 and 3 show constant current topographic images of the $Bi_2Se_3(0001)$ surface which were taken after dosing 1400 and 4200 L of hydrogen corresponding to $R = 0.23$ and 0.09, respectively. In Fig. 2, three terraces are visible. They are separated by two steps labeled by "Bi_2Se_3 step" whose heights are equal to 9.6 Å corresponding to the geometric step height of a Bi_2Se_3 QL which is equal to 9.54 Å [23]. One QL consists of a sequence of Se-Bi-Se-Bi-Se layers, while the whole crystal is composed of van-der-Waals bonded QLs.

On each terrace two areas labeled by "area1" and "area2" can be distinguished, in which the STM contrast is significantly different. This is clarified by the profiles along the lines labelled by "A" and "B" shown in Fig. 2(b). While for area1 the corrugation lies in the range of approximately 1 Å only, for area2 it is in the 3.5 to 4 Å regime suggesting the presence of BL islands. The boundary between the two regions runs parallel to the QL step edge. The apparent step height at

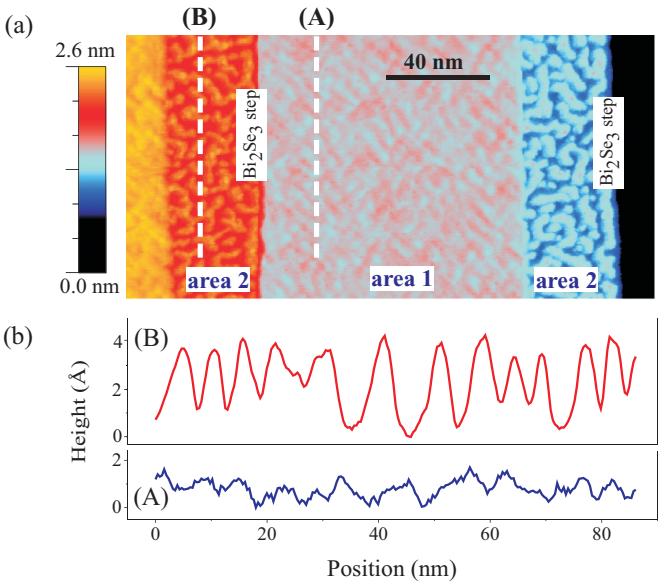

FIG. 2. (Color online) (a) 200 × 100 nm^2 STM topographic image ($U = 1$ V, $I = 200$ pA) of $Bi_2Se_3(0001)$ after exposure to 1400 L of hydrogen. Three terraces are observable separated by a 9.5 Å high step corresponding to the height of a quintuple layer labeled by "Bi_2Se_3 step." (b) Profiles along the lines labeled "A" and "B" within the region "area1" and "area2" characterized by low and high topographic contrast. Note that the profiles are set to height = 0 at their minima.

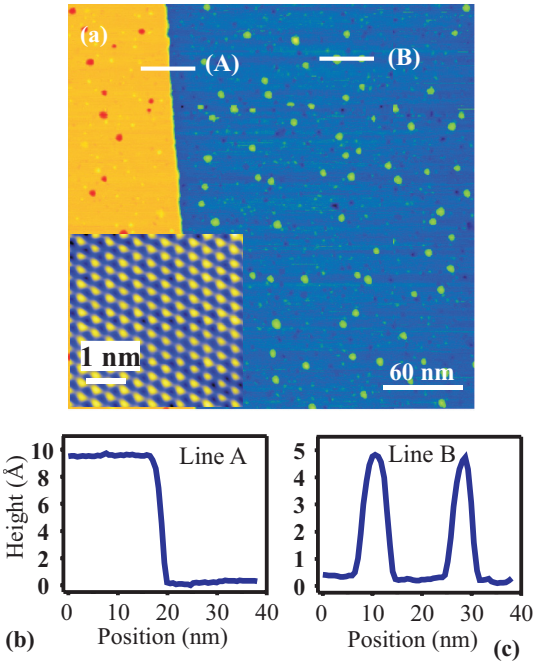

FIG. 3. (Color online) (a) Topographic STM image (300 × 300 nm^2, $U = 1$ V, $I = 200$ pA) of the topmost bismuth layer of the BL film on $Bi_2Se_3(0001)$ prepared by exposing Bi_2Se_3 to 4200 L of atomic hydrogen. Two profiles along the lines "A" and "B" are shown in (b) and (c), respectively. The inset shows an atomically resolved image of the bismuth surface.

the boundary between the two areas on one QL terrace is approximately 1.9 Å.

Prolonged dosing (4200 L, corresponding to $R = 0.09$) leads to the flattening of the surface morphology as shown in Fig. 3(a). Apart from a 9.5 Å high QL step atomically flat terraces are observed on which small islands, about 5 nm in diameter and 4.2 Å in height, are located [see line profiles in Figs. 3(b) and 3(c)]. Given the fact that after dosing of 4200 L of hydrogen the selenium AES signal has almost disappeared (see Fig. 1), it can be qualitatively concluded that at least the two topmost layers of the crystal are composed of bismuth. The atomically resolved image in the inset shows well ordered hexagonal arrangement of the top layer bismuth atoms.

Based on the STM image alone it is not possible to draw quantitative conclusions with regard to the detailed atomic surface structure. To this end, we have carried out quantitative SXRD experiments. SXRD benefits from the applicability of the single scattering theory, facilitating the quantitative analysis of the scattered intensities.

Solid symbols in Fig. 4 represent the experimental structure factor amplitudes ($|F_{\mathrm{obs}}(hk\ell)|$) along several CTRs collected for the $Bi_2Se_3(0001)$ sample after low (≈1200 L, upper curves) and high ($\approx 6 \times 10^4$ L, lower curves) hydrogen exposure. While the STM image of Fig. 2(a) was taken after a comparable exposure (1400 L) as applied for the SXRD experiment, it significantly differs for the highly dosed samples. However, as it will be shown below in comparison with the STM image in Fig. 3(a) (exposure 4200 L), prolonged dosing beyond the 4200 L range does not significantly affect the overall surface morphology and atomic structure since the SXRD

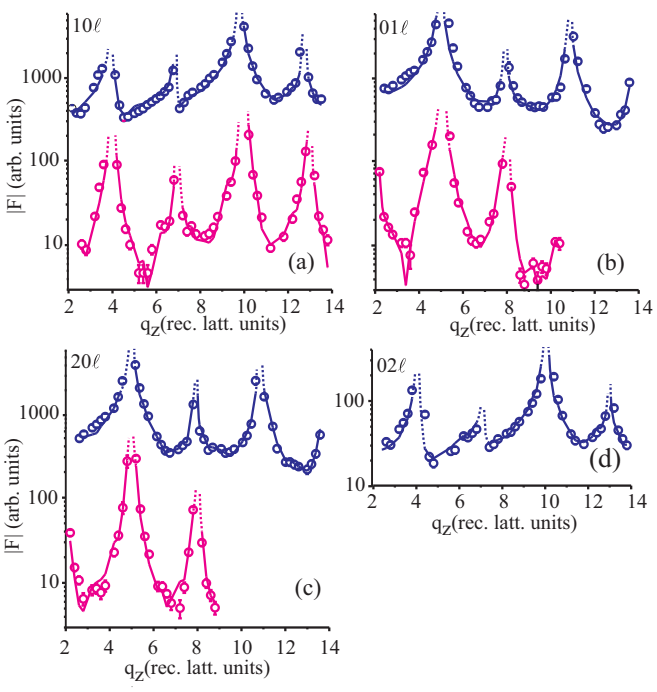

FIG. 4. (Color online) Experimental (symbols) and calculated (lines) structure factor amplitudes $|F|$ along crystal truncation rods of Bi_2Se_3 after low (upper curves) and high (lower curves) exposure to hydrogen. Curves are shifted by 100 units in $|F|$ for clarity. Fits correspond to structure models shown in Fig. 5.

derived structure model correlates well with the STM derived morphology.

The $|F_{\mathrm{obs}}(hk\ell)|$ were derived from the integrated intensities $I(hk\ell)$ with $|F_{\mathrm{obs}}(hk\ell)| \propto \sqrt{I(hk\ell)}$. They were collected by a 2D pixel detector and corrected for geometrical factors [24]. The CTRs appear due to the truncation of the crystal [25]. In the present case, where only rods related to the (1×1) substrate metric are present, the quantitative analysis of the adsorbate structure is based on the interference between the scattering amplitude of the semi-infinite substrate formally expressed by the structure factor $F_{\mathrm{sub}}(hk\ell)$ and that of the adsorbate, $F_{\mathrm{ad}}(hk\ell)$, given by $I(hk\ell) \propto |F_{\mathrm{sub}}(hk\ell) + F_{\mathrm{ad}}(hk\ell)\,\exp[i\phi]|^2$, where the phase factor formally accounts for the registry of the adsorbate structure relative to the substrate. The bulk substrate contribution can be written as a semi-infinite sum from $n \in [-\infty,0]$ over the number n of unit cells (uc) multiplied by the uc structure factor $F_{\mathrm{uc}}(hk\ell)$, leading to the expression $F_{\mathrm{sub}}(hk\ell) = F_{\mathrm{uc}}(hk\ell)\,1/[1 - \exp(-i2\pi\ell)]$. Adding the adsorbate contribution the relation $F_{tot} = F_{\mathrm{uc}}(hk\ell) \times 1/[1 - \exp(-i2\pi\ell)] + \sum f_j\,\theta_j\,\exp[i2\pi(hx_j + ky_j + lz_j)]$ is obtained, where the adsorbate contribution has been written in full generality including the atomic scattering factor (f_j), the occupancy (θ_j) and the atomic coordinates (x_j, y_j, z_j) of all atoms j located on the bulk truncated crystal. In this way, also relaxations of the substrate surface structure can be considered.

According to the hexagonal setting of the rhombohedral crystal structure bulk Bragg reflections appear at the condition $-h + k + \ell = 3m$ with $m \in \mathbf{Z}$. They are not included in the analysis, since the surface contribution is negligible there. Experimental uncertainties (1σ) were derived from the counting statistics and the reproducibility of symmetry equivalent reflections. In the present case, σ is in the range of 10%–15% in $|F|$. The $|F_{\mathrm{obs}}|$ along several symmetry independent CTRs were collected, namely 10ℓ, 01ℓ, 20ℓ, and 02ℓ [Figs. 4(a)–4(d)].

The structure analysis was carried out by fitting calculated structure factor amplitudes ($|F_{\mathrm{calc}}|$) to the observed ones using the program PROMETHEUS. [26] The analysis benefits from the fact that all atoms occupy high symmetry sites within the plane group $p3m1$. All atoms are located at threefold rotation axes. In consequence, there is no positional freedom within the $\vec{a}$-$\vec{b}$ plane and only the z-parameters (one per atomic layer) are allowed to vary. In addition, one overall Debye parameter $B = 8\pi\,\langle u^2\rangle$, where $\langle u^2\rangle$ represents the mean squared displacement amplitude, was refined.

The $|F_{\mathrm{calc}}|$, represented by solid lines in Fig. 4 are superimposed to the observed ones. From a direct inspection, it is evident that while the overall shape of the rods is very different for the two samples, the fits are very precise for both data sets. The fit quality is quantified by the unweighted residual (R_U), which is the average (relative) deviation of the $|F_{\mathrm{calc}}|$ from the $|F_{\mathrm{obs}}|$ given by $R_U = \sum ||F_{\mathrm{calc}}| - |F_{\mathrm{obs}}|| / \sum |F_{\mathrm{calc}}|$, where the summation runs over all data points. R_U values in the range from 0.12 to 0.15 are achieved.

Figure 5 schematically sketches the near surface structure of the Bi_2Se_3 crystal in side view after low (a) and high (b) hydrogen dosing. The structure models are exactly related to the fits shown in Fig. 4. In accordance with the STM image [see Fig. 2(a)], for low hydrogen dosing, two structurally

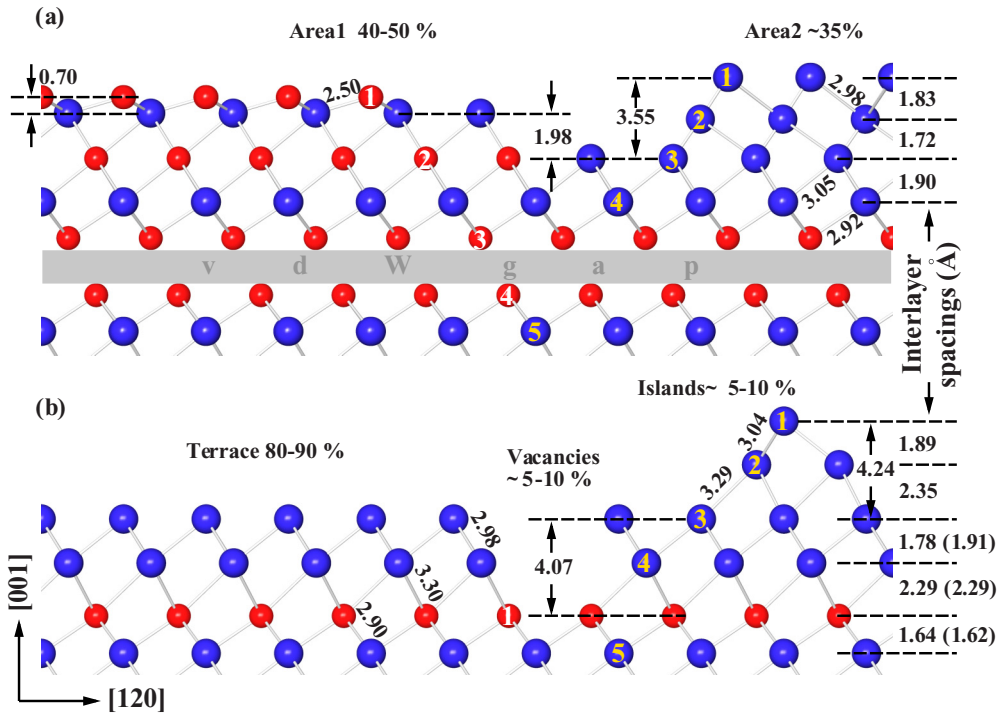

FIG. 5. (Color online) SXRD derived schematic structure models for the near surface region of Bi_2Se_3 after low (a) and high (b) exposure of hydrogen. Large blue and small red spheres correspond to bismuth and selenium atoms, respectively. Numbers label distances in angstrom units. Theoretically calculated interlayer spacings for the bismuth BL are shown in brackets in (b). The relative abundance of the different regions is indicated in percent of a monolayer. Bismuth and selenium layers are respectively labeled by yellow and white numbers beginning with "1" from the top.

different regions labeled by "area1" and "area2" are formed. The former, here with an abundance of about 50%, is characterized by an intact QL with selenium islands (selenium atoms "1") on the surface. These islands cover approximately 2/3 of the second bismuth layer. This explains why the selenium MMM AES peak is still observable. In area1, the STM contrast is low and given by the height difference (Δh) between the selenium atoms and the bismuth atoms underneath. The SXRD structure analysis finds $\Delta h \approx 0.7$ Å, which is in reasonable agreement with the STM corrugation (average approximately 1.0–1.2 Å). In comparison with the bulk vertical spacing (1.59 Å) [19] this corresponds to a reduction of -56%, but it should be emphasized, that the contraction of the selenium-bismuth bonds is much less dramatic and amounts to only -12% (2.50 Å versus 2.86 Å in the bulk). This bond length contraction is related to the finite size of the islands, which is commonly referred to as "mesoscopic misfit" [27]. The uncertainty of the determination of the vertical spacings lies in the 0.05 to 0.10 Å range.

While area1 can still be viewed as an intact $Bi_2Se_3(0001)$ surface albeit with a selenium deficiency, area2 corresponds to a region where the bismuth concentration is already considerably enriched. The SXRD model provides evidence that this part of the near surface region consists of bismuth islands composed of layers labeled "1" and "2." These bismuth islands on the right of Fig. 5(a) correspond to the BL visible in the STM image in Fig. 3(a), which are 3.55 Å high and reside on the bismuth layer "3." The step height between area1 and area2 is equal to 1.98 Å also in very good agreement with the STM experiment. It should be noted that in the present experiment the x-ray coherence length (≈30 nm) is smaller than the average terrace size, which is several hundred nm. Consequently, the substrate morphology characterized by its 9.5 Å steps can be neglected in the analysis (incoherent scattering from different terraces) and only the coherent scattering within the terraces plays a role for the scattered intensity.

In general the atomic species, bismuth ($Z = 83$) and selenium ($Z = 34$) can be well separated in x-ray diffraction since the atomic scattering amplitude is proportional to the atomic number Z. An important result of the combined STM and the SXRD analysis is that upon hydrogen dosing selenium is not only directly removed from the topmost surface but also laterally by penetration of hydrogen into the QLs from the step edges leading to a "reaction front" visible by the boundary between area1 and area2 which runs parallel to the step edge. This is responsible for the characteristic lateral asymmetry of the chemical composition, structure and morphology within each terrace.

The bismuth interlayer distances can be compared with those in bulk bismuth along the [111] direction [28,29], where a long (2.35 Å) and a short (1.59 Å) distance alternate corresponding to the strength of the interlayer bonds, which are of van der Waals and covalent type, respectively. A gross overview over the distances within the bismuth rich regime shows that they do not correspond to the bulk ones. We neither observe the characteristic sequence of the spacings nor any of the bulklike distances within the experimental uncertainty (≈0.10–0.15 Å). As compared to the short bulk

spacing (1.59 Å) those in the bismuth rich region are expanded by 10%–20% (1.83, 1.72, and 1.90 Å). Using elasticity theory a 10% expansion of the interlayer spacing can be explained by the in-plane compression of −8.8% along the hexagonal axes of the bismuth lattice on Bi_2Se_3(0001) (lattice parameter $a_0 = b_0 = 4.14$ Å on Bi_2Se_3 versus 4.54 Å in the bulk). In the hexagonal system, the out-of-plane lattice strain ε_3 is related to the in-plane strains ε_1 and ε_2 by $\varepsilon_3 = -(C_{13}/C_{33})(\varepsilon_1 + \varepsilon_2)$, were the C_{ij} are the experimental bulk elastic constants, and ε_i $(i = 1,2,3)$ represents the strain along the [210], [010], and [001] direction, respectively [30]. Using $C_{13} = 24.5$ GPa and $C_{33} = 38.1$ GPa from Ref. [31] we obtain an expansion of $\varepsilon_3 = +0.11$ in good agreement with the experimental data as far as the two upper spacings are concerned.

Prolonged exposure of hydrogen, i.e., beyond 4200 L, leads along with the disappearance of the selenium MMM transition in the AES spectrum to significant changes in the SXRD profiles (lower curves in Fig. 4) as well as in the STM image where a flattening of the surface morphology is observed [Fig. 3(a)]. The SXRD analysis (after dosing 6×10^4 L) confirms this result in all details. It can be concluded that the structural changes with respect to a 4200 L exposed sample are not significant. STM images show that the density of bismuth BL vacancies slowly increases with exposure.

Figure 5(b) schematically shows that the surface is composed of a *bismuth BL* covering about 80%–90% of the surface on a selenium terminated intact crystal. In addition, there is a fraction of double layer vacancies (≈5%–10%) and BL high (≈4 Å) bismuth islands, also observable in the STM image. The surface can be seen as being composed of the remainings of the first QL after three selenium layers of the top QL have been removed, i.e., a compact well ordered bismuth BL is left behind. The presence of an almost perfect bismuth BL even after prolonged exposure to hydrogen atoms indicates that the bismuth BL can be regarded as a protective layer which is significantly more resistant versus hydrogen exposure than selenium is. For practical preparation purposes, this is of considerable importance as no highly accurate calibration of the hydrogen dosage is necessary to prepare the bismuth BL.

We find that the vertical spacing within the BL located on the Bi_2Se_3(0001) surface (1.78 Å) is perfectly in agreement with the prediction from elasticity theory of $\varepsilon_3 = +0.11$ corresponding to 1.78 Å as discussed above. Furthermore, the large vertical spacing between the lower bismuth layer and the topmost selenium layer (2.29 Å) suggests a rather weak interaction with the Bi_2Se_3 substrate, which might be important for the stabilization of the 2D topological character of the bismuth BL, whose structure closely resembles the bulk one. In agreement with this suggestion, the characteristic sequence of layer spacings (long/short/long/...) even continues into the island structure (2.35 and 1.89 Å).

III. THEORY

Following the detailed experimental structure determination of the bismuth BL film on Bi_2Se_3, we went one step further to carry out first-principles calculations of the system to support the experimental results and to compare the calculated band structure with available experimental data. This was done by using the projector augmented-wave method [32] in the VASP implementation [33,34] and the generalized gradient approximation to the exchange-correlation potential [35]. The Hamiltonian contained the scalar relativistic corrections and the spin-orbit coupling was taken into account by the second variation method [36]. In order to correctly describe the van der Waals interactions we made use of the DFT-D2 approach [37].

The atomic positions, derived from the calculations, are in good agreement with the experimental ones [see Fig. 5(b) on the right in brackets]. Some disagreement only exists for the interlayer spacing within the bismuth BL, for which the theoretical value (1.91 Å) is about 7% larger then the experimental one (1.78 Å). This disagreement can be explained by the roughness of the real surface, which was not taken into account in the calculation. We emphasize that the variation of this interlayer spacing within ±7% does not change the surface band structure significantly.

We further examined the electronic properties of a single bismuth BL terminated Bi_2Se_3(0001) surface using the experimentally obtained atomic structure. We have found that the topological surface state (TSS) of the system features the Dirac point at about 0.27 eV below the Fermi level, almost in the middle of the bulk band gap [Fig. 6(a)]. The TSS maintains helical spin texture and is localized predominantly in the second QL of Bi_2Se_3(0001) as shown in Figs. 6(c)–6(d). This is at variance to the pristine surface, for which the Dirac state primarily resides in the first QL [38]. It should be noted that our calculated dispersion curves are in disagreement with those published by Eich *et al.* [39], who found a bismuth BL to be located 4.4 Å above the substrate. However, our results are in good agreement with those of two other recent theoretical studies concerning the band dispersion, Dirac cone spin texture and its real-space localization [40,41]. In addition, we find excellent agreement of our dispersion curves with experimental ones collected in a photoemission study by Miao *et al.* [41]. The data were taken from bismuth BL epitaxially grown on Bi_2Se_3(0001). This is emphasized in Fig. 6(b) by the direct comparison of the calculated (red lines) with the experimental band structure (triangles). In consequence, the experimentally derived atomic structure of the bismuth BL on the Bi_2Se_3(0001) surface is highly reliable. Finally, we would like to emphasize that, in comparison to epitaxial growth, the new procedure presented in this study allows to prepare the surface of significantly higher quality, almost without imperfections within the bismuth BL and with a smaller size of the second bismuth BL islands (cf. Fig. 3(a) of the present work and Fig. S1(J) in Ref. [41]).

IV. SUMMARY

In summary, we have presented an *in situ* top-down approach to prepare a flat long-range-ordered bismuth-bilayer-terminated Bi_2Se_3(0001) surface. While previous investigations used conventional techniques like cleaving, exfoliation or molecular beam epitaxy resulting in bilayers which were fairly limited in size, flatness and regularity of the step edges, our approach represents a step forward in that it creates a bilayer covered topological insulator by removing the chalcogen layers from the first quintuple layer in a top-down approach.

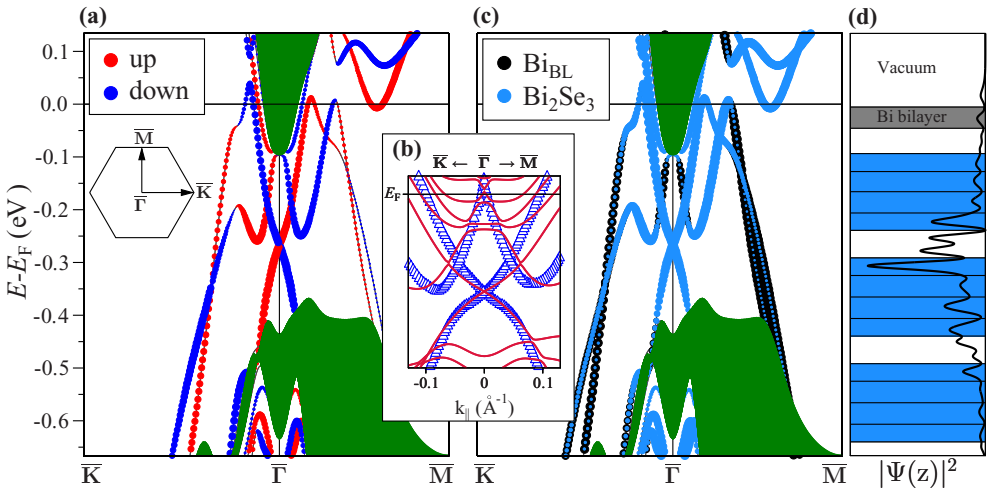

FIG. 6. (Color online) Surface energy band dispersion of a single bismuth BL terminated Bi_2Se_3(0001) with spin (a) and space (c) resolution. In (a), the spin component shown is oriented in-plane, perpendicular to the **k** vector. The color coding and size of the circles indicates the localization of the respective states, where black and blue correspond to the bismuth BL and the two topmost Bi_2Se_3(0001) QLs, respectively. Green-shaded areas correspond to the bulk band structure projected onto the surface Brillouin zone. (b) The calculated band structure (red lines) superimposed onto the experimental one (blue triangles) reproduced from Ref. [41], the latter being shifted upwards by 45 meV to align the Dirac points. (d) Spatial distribution of the Dirac cone charge density integrated over the (x, y) plane of the bismuth BL terminated Bi_2Se_3(0001).

This leads to a surface morphology, which is atomically flat and whose lateral size is only limited by the terrace size of the Bi_2Se_3 substrate. Our procedure appears to be applicable to more complicated 3D TIs which are composed of thicker building blocks (e.g., septuple or nine layer blocks), possibly allowing the creation of different metal overlayers on the TI serving as substrate. Furthermore, the presence of a flat and large size morphology also suggests the subsequent deposition of foreign atoms in a "bottom-up" type scheme allowing the preparation of novel TI architectures.

ACKNOWLEDGMENTS

This work is supported by the Deutsche Forschungsgemeinschaft through priority program SPP 1666 (Topological Insulators). We thank Frank Weiss for technical support. We also thank Z.S. Aliev, M. B. Babanly, K. A. Kokh, and O. E. Tereshchenko for providing samples. Calculations were performed on the SKIF-Cyberia supercomputer of Tomsk State University. M.M.O. and E.V.C. thank the Tomsk State University Academic D.I. Mendeleev Fund Program (Research Grant No. 8.1.05.2015).

[1] L. Fu and C. L. Kane, Topological insulators with inversion symmetry, Phys. Rev. B **76**, 045302 (2007).
[2] Y. Xia, D. Qian, D. Hsieh, L. Wray, A. Pal, H. Lin, A. Bansil, D. Grauer, Y. S. Hor, R. J. Cava, and M. Z. Hasan, Observation of a large-gap topological-insulator class with a single dirac cone on the surface, Nat. Phys. **5**, 398 (2009).
[3] D. Hsieh, D. Qian, L. Wray, Y. Xia, Y. S. Hor, R. J. Cava, and M. Z. Hasan, A topological dirac insulator in a quantum spin hall phase, Nature (London) **452**, 970 (2008).
[4] M. Z. Hasan and C. L. Kane, Colloquium: Topological insulators, Rev. Mod. Phys. **82**, 3045 (2010).
[5] H. Zhang, C.-X. Liu, X.-L. Qi, X. Dai, Z. Fang, and S.-C. Zhang, Topological insulators in Bi_2Se_3, Bi_2Te_3 and Sb_2Te_3 with a single dirac cone on the surface, Nat. Phys. **5**, 438 (2009).
[6] S. V. Eremeev, G. Landolt, T. V. Menshchikova, B. Slomski, Y. M. Koroteev, Z. S. Aliev, M. B. Babanly, J. Henk, A. Ernst, L. Patthey, A. Eich, A. A. Khajetoorians, J. Hagemeister, O. Pietzsch, J. Wiebe, R. Wiesendanger, P. M. Echenique, S. S. Tsirkin, I. R. Amiraslanov, J. H. Dil, and E. V. Chulkov, Atom-specific spin mapping and buried topological states in a homologous series of topological insulators, Nat. Commun. **3**, 635 (2012).
[7] *The Quantum Hall Effect*, edited by R. E. Prange, S. M. Grivin, and K. V. Klitzing (Springer, New York, 1986).
[8] B. A. Bernevig, T. L. Hughes, and S.-C. Zhang, Quantum spin hall effect and topological phase transition in HgTe qunatum wells, Science **314**, 1757 (2006).
[9] M. König, S. Wiedmann, C. Brüne, A. Roth, H. Buhmann, L. W. Molenkamp, X.-L. Qi, and S.-C. Zhang, Quantum spin hall insulator state in hgte quantum wells, Science **318**, 766 (2007).
[10] S. Murakami, Quantum spin hall effect and enhanced magneitc response by spin-orbit coupling, Phys. Rev. Lett. **97**, 236805 (2006).
[11] M. Wada, S. Murakami, F. Freimuth, and G. Bihlmayer, Localized edge states in two-dimensional insulators: Ultrathin Bi films, Phys. Rev. B **83**, 121310(R) (2011).
[12] T. Hirahara, G. Bihlmayer, Y. Sakamoto, M. Yamada, H. Miyazaki, S.-I. Kimura, S. Blügel, and S. Hasegawa, Interfacing 2d. and 3d. topological insulators: Bi(111) bilayer on Bi_2Te_3, Phys. Rev. Lett. **107**, 166801 (2011).

[13] M. Chen, J.-P. Peng, H.-M. Zhang, L.-L. Wang, K. He, X.-C. Ma, and Q.-K. Xue, Molecular beam epitaxy of bilayer Bi(111) films on topological insulator Bi2Te3: A scanning tunneling microscopy study, Appl. Phys. Lett. **101**, 081603 (2012).

[14] F. Yang, L. Miao, Z. F. Wang, M.-Y. Yao, F. Zhu, Y. R. Song, M.-X. Wang, J.-P. Xu, A. V. Fedorov, Z. Sun, G. B. Zhang, C. Liu, F. Liu, D. Qian, C. L. Gao, and J.-F. Jia, Spatial and energy distribution of topological edge states in single Bi(111) bilayer, Phys. Rev. Lett. **109**, 016801 (2012).

[15] S. H. Kim, K.-H. Jin, J. Park, J. S. Kim, S.-H. Jhi, T.-H. Kim, and H. W. Yeom, Edge and interfacial states in a two-dimensional topological insulator: Bi(111) bilayer on Bi_2Te_2Se, Phys. Rev. B **89**, 155436 (2014).

[16] C. Sabater, D. Gosálbez, J. Fernández-Rossier, J. G. Rodrigo, C. Untiedt, and J. J. Palacios, Topologically protected quantum transport in locally exfoliated bismuth at room temperature, Phys. Rev. Lett. **110**, 176802 (2013).

[17] I. K. Drozdov, A. Alexandradinata, S. Jeon, S. Nadj-Perge Ji, H. Cava, R. J. Bernevig, and B. A. Yazdani, A one-dimensional topological edge states of bismuth bilayers, Nat. Phys. **10**, 664 (2014).

[18] S. Roy. H. L. Meyerheim, A. Ernst, K. Mohseni, C. Tusche, M. G. Vergniory, T. V. Menshchikova, M. M. Otrokov, A. G. Ryabishchenkova, Z. S. Aliev *et al.*, Tuning the dirac point position in Bi_2Se_3(0001) via surface carbon doping, Phys. Rev. Lett. **113**, 116802 (2014).

[19] S. Roy. H. L. Meyerheim, K. Mohseni, A. Ernst, M. M. Otrokov, M. G. Vergniory, G. Mussler, J. Kampmeier, D. Grütmacher, C. Tusche *et al.*, Atomic relaxations at the (0001) surface of Bi_2Se_3(0001) single crystals and ultra thin films, Phys. Rev. B **90**, 155546 (2014).

[20] X. He, W. Zhou, Y. N. Wang, R. Q. Shi, and J. A. Yarmoff, Surface termination of cleaved Bi2Se3 investigated by low energy ion scattering, Phys. Rev. Lett. **110**, 156101 (2013).

[21] O. Waldmann and B. Ludewigt, Measurements of beam current density and proton fraction of a permanent-magnet microwave ion source, Rev. Sci. Instrum. **82**, 113505 (2011).

[22] E.-L. Zins and L. Krim, Hydrogenation processes from hydrogen peroxide: An investigation in Ne matrix for astrochemical purposes, RSC Adv. **4**, 22172 (2014).

[23] P. C. Vicente, J. L. Tirado, K. Adouby, J. C. Jumas, A. Abba Touré, and G. Kra, X-ray diffraction and ^{119}Sn Mössbauer spectroscopy study of a new phase in the Bi_2Se_3-SnSe system:$SnBi_4Se_7$, Inorg. Chem. **38**, 2131 (1999).

[24] C. M. Schlepütz, R. Herger, P. R. Willmott, B. D. Patterson, O. Bunk, Ch. Brönnimann, B. Henrich, G. Hülsen, and E. F. Eikenberry, Improved data acquisition in grazing-incidence x-ray scattering experiments using a pixel detector, Acta Crystallogr. Sect. A **61**, 418 (2005).

[25] I. K. Robinson, Crystal truncation rods and surface roughness, Phys. Rev. B **33**, 3830 (1986).

[26] U. H. Zucker, E. Perenthaler, W. F. Kuhs, R. Bachmann, and H. Schulz, PROMETHEUS. A program system for investigation of anharmonic thermal vibrations in crystals, J. Appl. Crystallogr. **16**, 358 (1983).

[27] O. O. Brovko, D. I. Bazhanov, H. L. Meyerheim, D. Sander, V. S. Stepanyuk, and J. Kirscher, Effect of misfit on growth, morphology, electronic properties and magnetism of nanostructures at metallic surfaces, Surf. Sci. Rep. **69**, 159 (2014).

[28] H. Mönig, J. Sun, Yu. M. Koroteev, G. Bihlmayer, J. Wells, E. V. Chulkov, K. Pohl, and Ph. Hofmann, Structure of the (111) surface of bismuth. leed analysis and-first principles calculations, Phys. Rev. B **72**, 085410 (2005).

[29] P. Hofmann, The surfaces of bismuth: Structural and electronic properties, Prog. Surf. Sci. **81**, 191 (2006).

[30] D. Sander, The correlation between mechanical stress and magnetic anisotropy in ultrathin films, Rep. Prog. Phys. **62**, 809 (1999).

[31] Y. Eckstein, A. W. Lawson, and D. Reneker, Elastic constants of bismuth, J. Appl. Phys. **31**, 1534 (1960).

[32] P. E. Blöchl, Projector augmented-wave method, Phys. Rev. B **50**, 17953 (1994).

[33] G. Kresse and J. Furthmüller, Efficient iterative schemes for ab initio total-energy calculations using a plane-wave basis set, Phys. Rev. B **54**, 11169 (1996).

[34] G. Kresse and D. Joubert, From ultrasoft pseudopotentials to the projector augmented-wave method, Phys. Rev. B **59**, 1758 (1999).

[35] J. P. Perdew, K. Burke, and M. Ernzerhof, Generalized gradient approximation made simple, Phys. Rev. Lett. **77**, 3865 (1996).

[36] D. D. Koelling and B. N. Harmon, A. technique for relativistic spin-polarised calculations, J. Phys. C **10**, 3107 (1977).

[37] S. Grimme, Semiempirical GGA-type density functional constructed with a long-range dispersion correction, J. Comput. Chem. **27**, 1787 (2006).

[38] T. V. Menshchikova, M. M. Otrokov, S. S. Tsirkin, D. A. Samorokov, V. V. Bebneva, A. Ernst, V. M. Kuznetsov, and E. V. Chulkov, Band structure engineering in topological insulator based heterostructures, Nano Lett. **13**, 6064 (2013).

[39] A. Eich, M. Michiardi, G. Bihlmayer, X.-G. Zhu, J.-L. Mi, B. Bo. Iversen, R. Wiesendanger, Ph. Hofmann, A. A. Khajetoorians, and J. Wiebe, Intra-and interband electron scattering in a hybrid topological insulator: bismuth bilayer on Bi_2Se_3, Phys. Rev. B **90**, 155414 (2014).

[40] K. Govaerts, K. Park, C. De Beule, B. Partoens, and D. Lamoen, Effect of Bi bilayers on the topological states of Bi_2Se_3: A first-principles study, Phys. Rev. B **90**, 155124 (2014).

[41] L. Miao, Z. F. Wang, W. Ming, M.-Y. Yao, M. Wang, F. Yang, Y. R. Song, F. Zhu, A. V. Fedorov, Z. Sun, C. L. Gao, C. Liu, Q.-K. Xue, C.-X. Liu, F. Liu, D. Qian, and J.-F. Jia, Quasiparticle dynamics in reshaped helical dirac cone of topological insulators, Proc. Natl. Acad. Sci. USA **110**, 2758 (2013).